Journal of Hazardous Materials 217–218 (2012) 422–428

Contents lists available at SciVerse ScienceDirect

Journal of Hazardous Materials

journal homepage: www.elsevier.com/locate/jhazmat

Bi_2MoO_6 ultrathin nanosheets on $ZnTiO_3$ nanofibers: A 3D open hierarchical heterostructures synergistic system with enhanced visible-light-driven photocatalytic activity

Peng Zhang, Changlu Shao*, Mingyi Zhang, Zengcai Guo, Jingbo Mu, Zhenyi Zhang, Xin Zhang, Yichun Liu

Center for Advanced Optoelectronic Functional Materials Research and Key Laboratory of UV Light-Emitting Materials and Technology of Ministry of Education, Northeast Normal University, 5268 Renmin Street, Changchun 130024, People's Republic of China

ARTICLE INFO

Article history:
Received 15 February 2012
Received in revised form 18 March 2012
Accepted 19 March 2012
Available online 28 March 2012

Keywords:
Electrospinning
$Bi_2MoO_6/ZnTiO_3$
Heterostructures
Photocatalytic
Recyclability

ABSTRACT

The 3D open $Bi_2MoO_6/ZnTiO_3$ hierarchical heterostructures with Bi_2MoO_6 ultrathin nanosheets (<10 nm) grown on hexagonal-phase $ZnTiO_3$ nanofibers were fabricated by combining the electrospinning technique and solvothermal method. And, the $Bi_2MoO_6/ZnTiO_3$ hierarchical heterostructures had remarkable light absorption in the visible region. The photocatalytic studies revealed that the hierarchical heterostructures system exhibited exceptional photocatalytic activity in visible-light degradation of Rhodamine B, which might be attributed to the synergistic system with excellent charge separation characteristics and the unique morphology of Bi_2MoO_6 nanosheets with the extended absorption in the visible light region. What is more, the 3D open structure supported on nanofibrous candidates possessed large surface areas and excellent recyclability.

1. Introduction

Semiconductors of the Aurivillius oxides with general formula $Bi_2A_{n-1}B_nO_{3n+3}$ (A = Ca, Sr, Ba, Pb, Na and B = Ti, Nb, Ta, Mo, W) have received extensive interests in solar energy conversion and degradation of pollution due to their layered structure and excellent intrinsic physical and chemical properties [1–3]. In particular, Bi_2MoO_6 as a typical Aurivillius oxide (the simplest member when $n = 1$), with a typical E_g of about 2.6 eV, shows great potential in the utilization of visible-light-active photocatalysts [4–6]. However, similar to other photocatalysts, poor quantum yield caused by the rapid recombination of photogenerated electrons and holes is still a challenge to enhancing the photocatalytic efficiency of Bi_2MoO_6 to meet the practical application requirements. Therefore, several attempts have been made to reduce the recombination of photoinduced electron–hole pairs by conjugation of the Bi_2MoO_6 with electron scavenging agents such as functional carbonaceous materials, metals, or metal-oxide-semiconductor (MOS) [7–9]. Among these, the manipulation of MOS heterostructures has proved to be an effective method in our previous work [10–12]. The coupling of two different semiconductors could transfer electrons from an excited narrow band gap semiconductor into another attached one in the case of proper conduction band (CB) potentials. Therefore, it is desirable to find a semiconductor which possessed a matchable bandgap to form the heterojunctions with Bi_2MoO_6.

Notably, titanium-based perovskite oxides of $A^{II}Ti^{IV}O_3$ type, where A is Pb, Sr, Ba, Zn or Fe, have attracted wide-spread attention due to their outstanding potential in photocatalysis because of their higher reduction potential and lower oxidation potential [12,13]. Especially, $ZnTiO_3$ with a hexagonal structure (h-$ZnTiO_3$) has a typical E_g of about 3.1 eV, which is wider than that of Bi_2MoO_6, but the CB of $ZnTiO_3$ is lower than that of Bi_2MoO_6. When radiated by visible light, the photogenerated electrons of Bi_2MoO_6 may move to the CB of $ZnTiO_3$, thus hindering the charge recombination and improve the photocatalytic efficiency. On the contrary, the candidates with one dimensional structure have been proved to be beneficial to the separation of the nanostructural photocatalysts from the solution [14–16]. Based on the above analysis, the $ZnTiO_3$ nanofibers ($ZnTiO_3$ NFs) may be a good candidate to form the one dimensional heterojunctions with Bi_2MoO_6.

In this paper, we had fabricated the $ZnTiO_3$ NFs with one dimensional structure by electrospinning technology, and had prepared the 3D open $Bi_2MoO_6/ZnTiO_3$ hierarchical heterostructures by using the electrospun $ZnTiO_3$ NFs as supports through solvothermal processing. The two-component hierarchical heterostructures synergistic system with excellent charge separation characteristics

* Corresponding author. Tel.: +8 6 4315098803.
E-mail address: clshao@nenu.edu.cn (C. Shao).

0304-3894/$ – see front matter © 2012 Elsevier B.V. All rights reserved.
doi:10.1016/j.jhazmat.2012.03.046

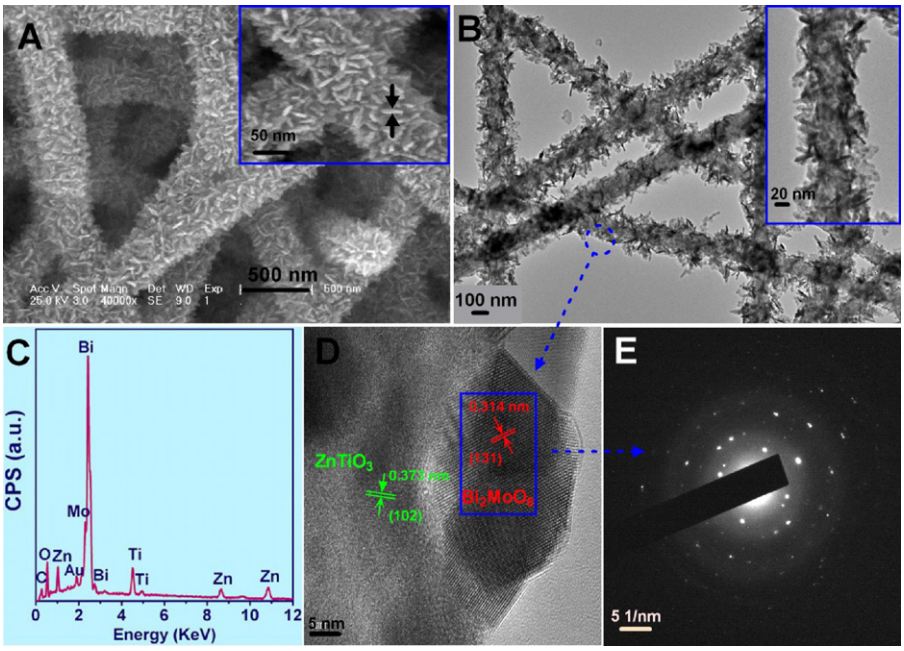

Fig. 1. (A) FESEM image of S1; (B) TEM image of S1; (C, D, E) EDX, HRTEM and SAED images of S1.

showed preeminent activity in the visible-light-driven photodegradation of Rhodamine B (RhB). What is more, the 3D open structure supported on nanofibrous candidates possessed large surface areas and excellent recyclability.

2. Experimental

2.1. Fabrication of $ZnTiO_3$ nanofibers

Firstly, 1.0 g of $Ti(OC_4H_9)_4$ and 0.65 g of ZnAc were dissolved in 5 mL of DMF and 2.5 mL of anhydrous ethanol. 0.5 g of PVP was added into the solution to increase the viscidity. Secondly, the mixture was magnetically stirred for 12 h at room temperature (RT) to form a homogeneous precursor solution. In this solution, the molar ratio between Zn and Ti is 1: 1. In a typical electrospinning process, the precursor solution was loaded into a plastic syringe equipped with a 23-gauge stainless needle. A high voltage of 20 kV was supplied by a direct-current power supply and the feeding rate for the precursor solution was adjusted to a constant rate of 0.3 mL h^{-1} by using a syringe pump. A piece of aluminum foil was placed at 15 cm below the tip of the needle to collect the as-spun nanofibers. The process was carried out in air at RT. For the following thermolysis process, the as-spun nanofibers were placed in a muffle furnace and calcined at 800 °C in air for 3 h with a heating rate of 2 °C min^{-1}, to remove PVP and obtain $ZnTiO_3$ nanofibers ($ZnTiO_3$ NFs).

2.2. Fabrication of $Bi_2MoO_6/ZnTiO_3$ hierarchical nanostructures

In a typical experiment, 421 mg $Bi(NO_3)_3{\cdot}5H_2O$ and 105 mg $Na_2MoO_4{\cdot}2H_2O$ were dissolved in 5 mL of ethylene glycol under magnetic stirring, respectively. The two solutions and $ZnTiO_3$ NFs (15 mg) were mixed together, and then 30 mL ethanol was slowly added into the above solution, followed by stirring for 10 min. The resulting clear solution (pH 7) was transferred into a 50 mL Teflon-lined stainless steel autoclave, which was heated to 160 °C and maintained for 24 h. Then, the autoclave was cooled down to room temperature. The obtained composite nanofibers were washed with deionized water and ethanol to remove any ionic residual then dried in oven at 80 °C for 4 h. The as-fabricated sample was denoted as S1. By tuning the precursor concentration for synthesizing Bi_2MoO_6, another sample of $Bi_2MoO_6/ZnTiO_3$ was fabricated and was denoted as S2. And, the Bi_2MoO_6 synthesized in the absence of $ZnTiO_3$ NFs was synthesized. The detailed experimental conditions for the fabrication of S1 and S2 were listed in Table S1 in ESI†. In addition, for simplicity, pure $ZnTiO_3$ NFs were denoted as S0.

2.3. Characterization

The morphologies of the as-prepared nanofibers were observed by the scanning electron microscope (SEM; XL-30 ESEM FEG, Micro FEI Philips), transmission electron microscopy (TEM; Hitachi 600). X-ray diffraction (XRD) measurements were carried out using a D/max 2500 XRD spectrometer (Rigaku) with Cu Kα line of 0.1541 nm. X-ray photoelectron spectroscopy (XPS) was accomplished using a PHI-5702 multi-functional X-ray photoelectron spectrometer with pass energy of 29.35 eV and an Mg Kα line excitation source. The specific surface areas of the samples were measured with a Micromeritics ASAP 2010 instrument and analyzed

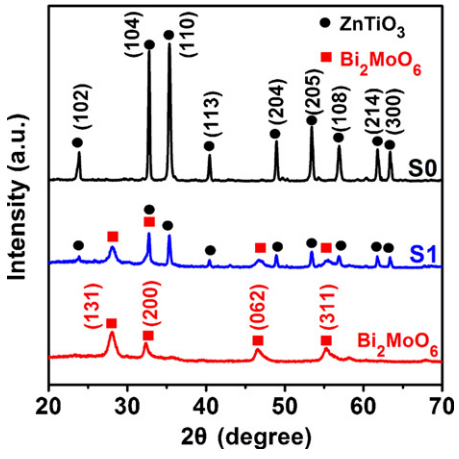

Fig. 2. XRD patterns of S0, S1 and pure Bi_2MoO_6.

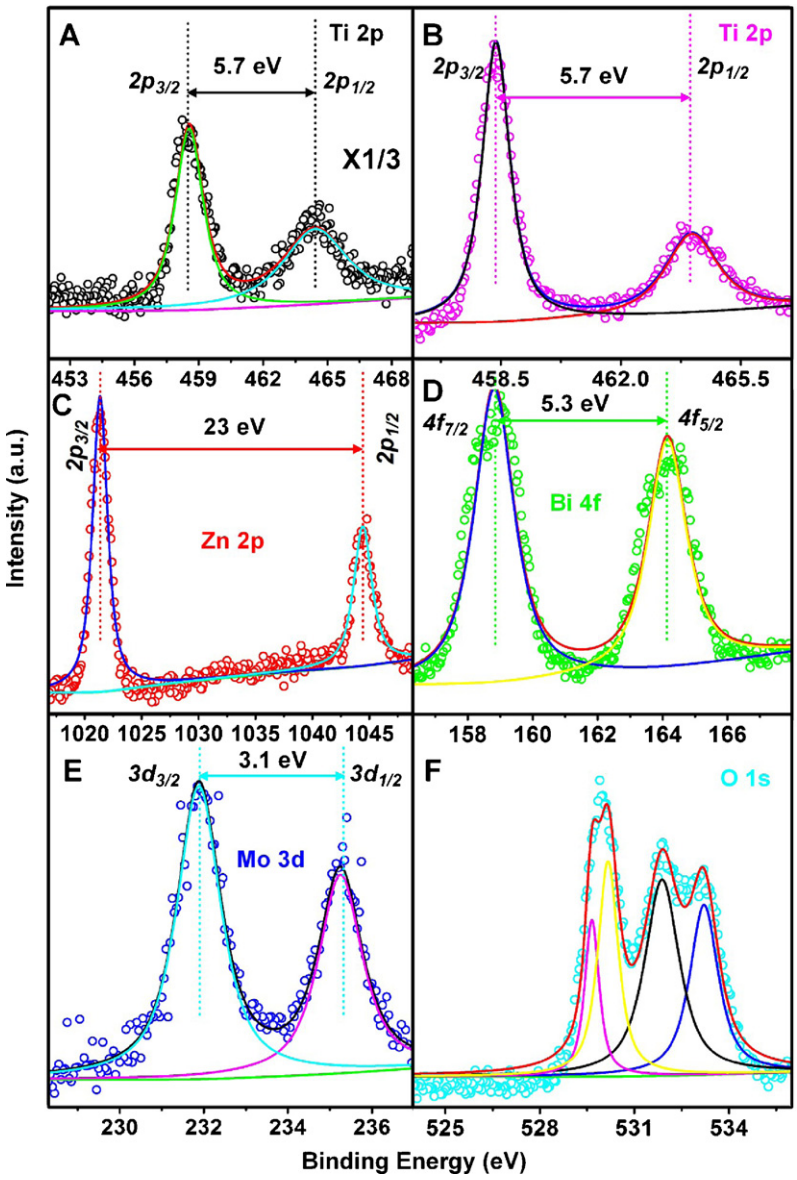

Fig. 3. (A, B) XPS spectra of Ti 2p for the samples S0 and S1; (C) XPS spectra of Zn 2p for the sample S1; (D) XPS spectrum of Bi 4f for the sample S1; (E) XPS spectra of Mo 3d for the sample S1; (F) XPS spectrum of O 1s for the sample S1.

by the BET method. The UV–vis diffuse reflectance (DR) spectroscopy of the samples was recorded on a Cary 500 UV–vis-NIR spectrophotometer.

2.4. Photocatalytic test

The photoreactor was designed with an internal xenon lamp (XHA 150 W) equipped with a cut-off glass filter transmitting $\lambda > 420$ nm surrounded by a water-cooling quartz jacket to cool the lamp, where a 100.0 mL of RB solution with an initial concentration of 10 mg L^{-1} in the presence of solid catalyst (0.05 g), respectively. The solution was stirred in the dark for 30 min to obtain a good dispersion and reach adsorption–desorption equilibrium between the organic molecules and the catalyst surface. Decreases in the concentrations of dyes were analyzed by a Cary 500 UV–vis-NIR spectrophotometer at $\lambda = 554$ nm. At given intervals of illumination, the samples (3 mL) of the reaction solution were taken out and centrifuged. Finally, the filtrates were analyzed.

3. Results and discussion

The morphology of the $Bi_2MoO_6/ZnTiO_3$ hierarchical heterostructures were analyzed by SEM and TEM. As displayed in Fig. 1(A), ultrathin (<10 nm) Bi_2MoO_6 nanosheets branched uniformly on the surface of $ZnTiO_3$ NFs. In contrast, the pure $ZnTiO_3$ NFs (Fig. S1 in ESI†) ranged from 60 to 100 nm were of relative smooth surface without secondary structures. The TEM image of the S1 further verified that the Bi_2MoO_6 nanosheets with well-dispersed distribution grew along the nanofibers (Fig. 1B). And, EDX spectrum of S1 was measured to determine the chemical composition of the heterostructure. The existence of Zn, O, Ti, Bi and Mo elements was detected. It was worth pointing out that the atomic ratio of Zn to Ti was about 1:1 (Fig. S1 in ESI†), indicating the well defined $ZnTiO_3$ NFs through electrospinning technique. The HRTEM image from the heterostructures displayed two types of clear lattice fringes shown in Fig. 1D. One set of the fringes spacing was ca. 0.373 nm, corresponding to the (1 0 2) plane of h-$ZnTiO_3$. Another set of the fringes spacing measures ca. 0.314 nm, corresponding to the (1 3 1) lattice spacing of the orthorhombic phase of Bi_2MoO_6.

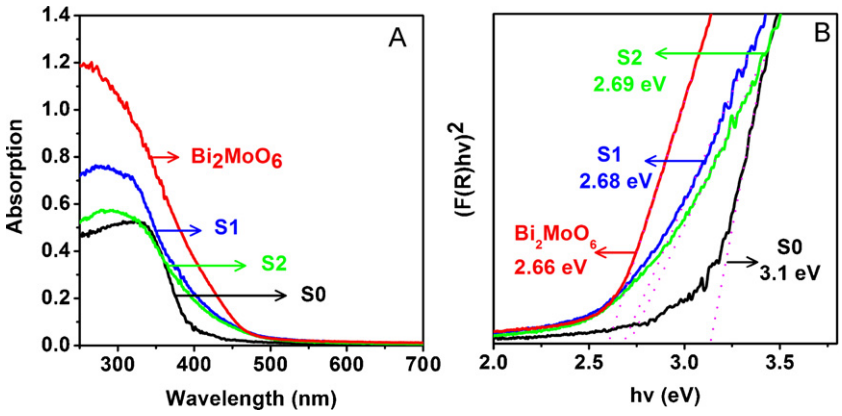

Fig. 4. (A) UV–vis diffuse reflectance spectra of S0, S1, S2 and Bi_2MoO_6. (B) Plots of $(F(R)h\nu)^2$ vs. $(h\nu)$ for estimation of the optical band gaps of S0, S1, S2 and Bi_2MoO_6.

Selected-area electron diffraction (SAED) pattern (Fig. 1E) from single nanosheet clearly demonstrated the high crystallinity of the nanosheet.

The XRD patterns (Fig. 2) were employed to investigate the crystal phase of $ZnTiO_3$ NFs (S0) and $Bi_2MoO_6/ZnTiO_3$ hierarchical heterostructures (S1). For the S1, diffraction peaks at about $2\theta = 24.1^\circ$, 32.8°, 35.3°, 40.5°, 48.8°, 52.9°, 56.8°, 61.7° and 63.3° could be perfectly indexed to the (1 0 2), (1 0 4), (1 1 0), (1 1 3), (2 0 4), (2 0 5), (1 0 8), (2 1 4) and (3 0 0) crystal faces of h-$ZnTiO_3$ (JCPDS 14-33), respectively. Besides, additional diffraction peaks with 2θ values of 28.1°, 32.3°, 34.6°, 46.7° and 55.3° appeared, corresponding to (1 3 1), (2 0 0), (0 6 0), (0 6 2) and (3 1 1) crystal planes of orthorhombic phase Bi_2MoO_6, respectively (JCPDS 76-2388). No other phases can be found in the S1, suggesting that no impurity species were formed between $ZnTiO_3$ and Bi_2MoO_6.

In order to further study the interaction and arrive at more detailed information regarding the chemical and bonding environment of the $ZnTiO_3$ and Bi_2MoO_6, XPS was applied. Fig. 3(A and B) showed XPS spectra of Ti 2p for the samples S0 and S1, there were two peaks in the Ti 2p region. The peak located at 464.2 eV corresponded to the Ti $2p_{1/2}$ and another one located at 458.6 eV was assigned to Ti $2p_{3/2}$. The splitting between Ti $2p_{1/2}$ and Ti $2p_{3/2}$ was 5.7 eV, indicating a normal state of Ti^{4+} in the as-prepared $Bi_2MoO_6/ZnTiO_3$ hierarchical nanostructures. Besides, the peaks for Ti 2p in the S1 showed no shift compared with that in pure S0, confirming that the structure of $ZnTiO_3$ remained intact after synthesis of Bi_2MoO_6. As observed in Fig. 3C, there were two symmetric peaks in the Zn 2p region. The peak centered at 1021.6 eV corresponded to the Zn $2p_{3/2}$ and another one centered at 1044.6 eV was assigned to Zn $2p_{1/2}$, indicating a normal state of Zn^{2+} in the

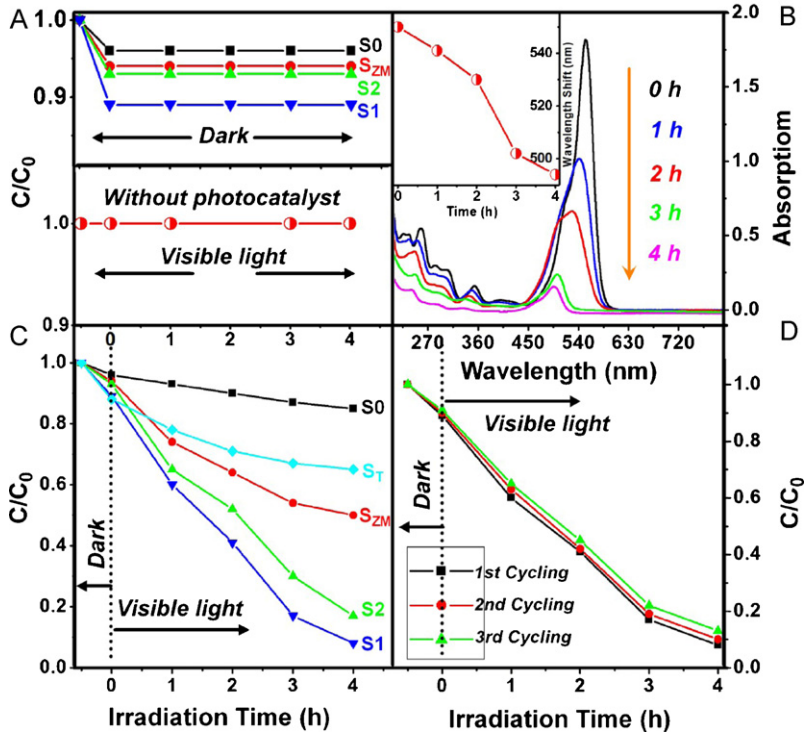

Fig. 5. (A) Degradation profiles of RB in the dark and self-degradation of RB with visible light irradiation but in the absence of the nanofiber photocatalysts. (B) UV–visible spectra of RhB vs. photoreaction time; wavelength shifts as a function of the decrease in absorption maximum (inset). (C) Degradation profiles of RB over different samples ($C = 10\,mg\,L^{-1}$, sample = 0.05 g). (D) Photocatalytic activity of S1 for RB degradation with three times of cycling uses.

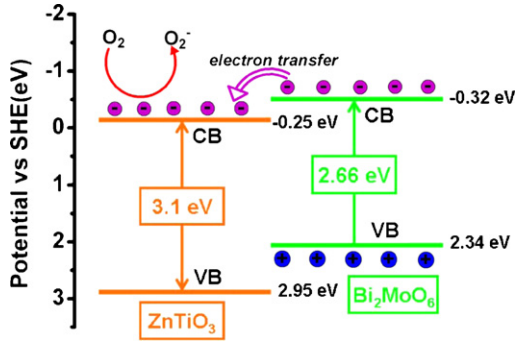

Fig. 6. A simplified band structure diagram for Bi_2MoO_6 and $ZnTiO_3$.

S1. Fig. 3D revealed the binding energies are 157.8 and 163.1 eV for Bi $4f_{7/2}$ and Bi $4f_{5/2}$, respectively. As for the Fig. 3E, the binding energies of around 232.2 eV and 235.3 eV could be ascribed to Mo 3d. Fig. 3E presented the spectra of O 1s for the $Bi_2MoO_6/ZnTiO_3$. The wide and asymmetric peak of the O 1s spectrum indicated that there might be more than one chemical state according to the binding energy. The peaks at 529.6 eV, 530.9 eV, 531.8 eV and 533.7 eV related to Bi–O (lattice O), Ti–O (lattice O), Zn–O (lattice O) and surface hydroxyl groups (O–H), respectively. The above XRD and XPS results confirmed the coexistence of Bi_2MoO_6 and $ZnTiO_3$ in the $Bi_2MoO_6/ZnTiO_3$ composites. The Bi species might not be incorporated into the $ZnTiO_3$ lattice because of the low-temperature synthetic conditions and the bigger size of the Bi atom (103 pm) than that of the Ti atom (61 pm), which inhibit the replacement of Ti by Bi in the TiO_2 crystal lattice.

In order to further study the photocatalytic performance of the $Bi_2MoO_6/ZnTiO_3$ hierarchical heterostructures, S2 was prepared. When the concentration of precursor $Bi(NO_3)_3$ was decreased, the morphology of Bi_2MoO_6 nanostructures grew on $ZnTiO_3$ nanofibers changed from nanosheets to nanoparticles (Fig. S2 in ESI†). Fig. 4 showed UV–vis diffuse reflectance spectra of the $ZnTiO_3$ nanofibers and as-prepared Bi_2MoO_6/TiO_2 hierarchical heterostructures. The spectrum of the $ZnTiO_3$ nanofibers exhibited the typical absorption behavior of a wide-band-gap oxide semiconductor, having an intense absorption band with a steep edge at about 400 nm. For the $Bi_2MoO_6/ZnTiO_3$ heterostructures, the curves of samples S1 and S2 showed significant red-shift of the absorption edge. For a crystalline semiconductor, the optical absorption near the band edge follows the equation:

$$ah\nu = A(h\nu - E_g)^{n/2}$$

where α, ν, E_g and A are the absorption coefficient, the light frequency, the band gap and a constant, respectively. Among them, n decides the characteristics of the transition in a semiconductor. In this work, the band gap of the pure Bi_2MoO_6 is calculated to be about 2.66 eV, while the band gap of $ZnTiO_3$ is found to be about 3.1 eV. It was found that the band gap of $Bi_2MoO_6/ZnTiO_3$ heterostructures were 2.68 or so. The decrease of band gap possibly leads to better photocatalytic efficiency, especially under visible-light irradiation.

Since the S1, S2 had remarkable light absorption in the visible region, we hoped that the $Bi_2MoO_6/ZnTiO_3$ hierarchical heterostructures present photochemical activity in the visible light region. As observed in Fig. 5A, the control experiments illuminated that the adsorption–desorption equilibrium of RB in the dark was established within 30 min. And, RhB itself was not decomposed in the absence of the photocatalysts. Fig. 5B showed the absorption spectra variation of RhB vs. irradiation time on the S1. The characteristic absorption band of RhB at 554 nm diminished quickly, accompanied by slight concomitant blue-shift from 554 to 494 nm of the maximum absorption. Fig. 5C showed the degradation curves of RB on the Degussa-P25 (S_T), pure $ZnTiO_3$ NFs (S0), mechanically mixed Bi_2MoO_6 and $ZnTiO_3$ NFs (S_{ZM}) and

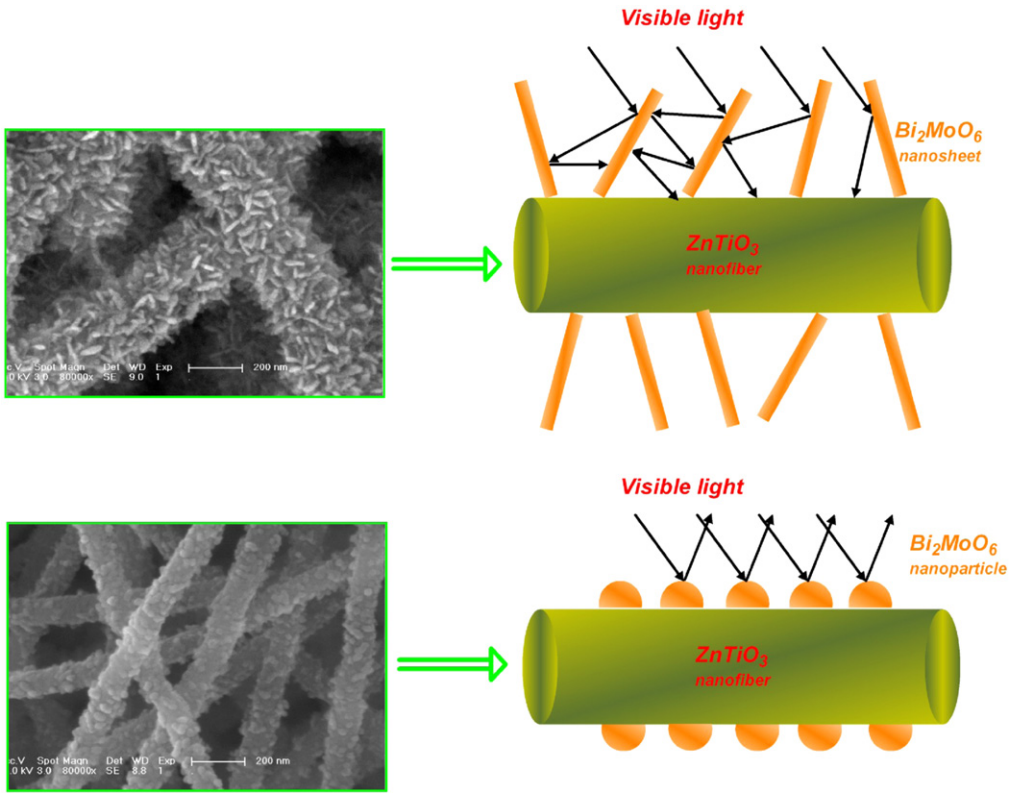

Fig. 7. Schematic illustration of multireflections within the S1 compared with S2.

$Bi_2MoO_6/ZnTiO_3$ hierarchical nanostructures (S1, S2). The photodegradation of RhB on P25 can be attributed to dye-sensitized photocatalysis. And, pure $ZnTiO_3$ NFs showed weak reactivity, on which less than 20% RhB was decomposed in 4 h irradiation, since $ZnTiO_3$ could not be activated by visible light. And, S_{ZM}, S1 and S2 displayed good photocatalytic activity under visible light irradiation; the degradation efficiency of RB was about 51, 91, and 82% after 4 h, respectively. It could be seen that $Bi_2MoO_6/ZnTiO_3$ hierarchical nanostructures exhibited high photocatalytic efficiency compared with the mechanically mixed Bi_2MoO_6 and $ZnTiO_3$ NFs. The order of photocatalytic activities is $S1 > S2 > S_{ZM}$. Moreover, from Fig. 3D, it was indicated that the S1 photocatalysts with high photocatalytic activity could be easily recovered by sedimentation because of the special one-dimensional structure.

The enhanced photocatalytic performance of S1 may be due to the following correlated factors: firstly, the Brunauer–Emmett–Teller (BET) surface area of the $Bi_2MoO_6/ZnTiO_3$ hierarchical nanostructures is estimated to be about 30.91 $m^2\,g^{-1}$, which is much higher than that of the pure $ZnTiO_3$ (19.01 $m^2\,g^{-1}$). The high surface area in the hierarchical heterostructure allows not only more surface to be reached by the incident light but also more active catalytic sites, which results in the good photocatalytic performance [17,18]. Secondly, the heterostructures formed between Bi_2MoO_6 and $ZnTiO_3$ is more effective in the suppression of electron–hole recombination.

Based on the above results, a possible synergetic mechanism was indicated. As depicted in Fig. 6, the band potentials of Bi_2MoO_6 and $ZnTiO_3$ in the heterostructures fit the requirements to form a heterojunction with a straddling gap, which may facilitate the transfer of charge carriers and retard the $e^- - h^+$ recombination, leading to the improved photocatalytic performance. The potentials of conductance and valence band (VB) edges of Bi_2MoO_6 and $ZnTiO_3$ were estimated via Mulliken electronegativity theory [19]:

$$E_{VB} = X_{semiconductor} - E^0 + 0.5E_g$$

where E_{VB} is the VB edge potential, $X_{semiconductor}$ is the electronegativity of the semiconductor, which is the geometric mean of the electronegativity of the constituent atoms, E^0 is the standard electrode potential on the hydrogen scale (ca. 4.5 eV). E_g was derived from $E_g = 1239.8/\lambda_g$, where λ_g is the absorption edge in the UV–vis spectra (Fig. 4). Bi_2MoO_6 as a sensitizer with narrow band gap energy (2.66 eV in this work) could be easily excited by visible light ($\lambda > 420$ nm, energy less than 2.95 eV), electrons in the VB of Bi_2MoO_6 could be excited up to a higher potential edge (−0.32 eV) [20,21]. The CB edge potential of Bi_2MoO_6 is active than that of $ZnTiO_3$ (−0.25 eV), in such a way, the photoinduced electron–hole pairs could be effectively separated. Moreover, the formed junction between Bi_2MoO_6 and $ZnTiO_3$ could further prevent the recombination between photoelectrons and holes. The generated conduction band electrons (e^-) probably reacted with dissolved oxygen molecules to yield superoxide radical anions, O_2^-, which on protonation generated the hydroperoxy, $HO_2^\bullet$, radicals, producing hydroxyl radical $OH^\bullet$, which was a strong oxidizing agent to decompose the organic dye. Meanwhile, since the Bi_2MoO_6 (h^+) radicals had a redox potential of about 2.34 V vs. NHE, it could oxidize a suitable substrate (R), together with recovery of the original Bi_2MoO_6. On the contrary, in the hierarchical heterostructures system, S1 exhibited better photocatalytic activity than S2. We believe that the morphology of Bi_2MoO_6 might also play an important role in the photocatalytic efficiency. As schematically illustrated in Fig. 7, compared with nanoparticles (S2), the unique hierarchical heterostructure with an appropriate space between the nanosheets (S1) allows multiple reflections of electromagnetic waves [22], such as visible light, thus allowing more efficient use of the light source and therefore endowing these hierarchical heterostructure fabrics with greatly enhanced properties [23].

In summary, the $Bi_2MoO_6/ZnTiO_3$ hierarchical heterostructures with ultrathin Bi_2MoO_6 nanosheets on $ZnTiO_3$ NFs showed exceptional visible-light-driven photocatalytic activity, which might be attributed to the synergistic system with excellent charge separation characteristics and the unique morphology of Bi_2MoO_6 nanosheets. What is more, the 3D open structure supported on nanofibrous candidates could be easily recycled. Also, the novel hierarchical heterostructure was expected to promote their industrial application to eliminate the organic pollutants.

Acknowledgments

The present work is supported financially by the National Natural Science Foundation of China (nos. 50572014, 50972027, and 10647108) and the Program for New Century Excellent Talents in University (NCET-05-0322).

Appendix A. Supplementary data

Supplementary data associated with this article can be found, in the online version, at doi:10.1016/j.jhazmat.2012.03.046.

References

[1] M. Shang, W.Z. Wang, J. Ren, S.M. Sun, L. Wang, L. Zhang, A practical visible-light-driven Bi_2WO_6 nanofibrous mat prepared by electrospinning, J. Mater. Chem. 19 (2009) 6213–6218.
[2] Z. Zhang, W. Wang, M. Shang, W. Yin, Low-temperature combustion synthesis of Bi_2WO_6 nanoparticles as a visible-light-driven photocatalyst, J. Hazard. Mater. 177 (2010) 1013–1018.
[3] Q.C. Xu, Y.H. Ng, Y. Zhang, J.S.C. Loo, R. Amal, T.T.Y. Tan, A three-way synergy of triple-modified Bi_2WO_6/Ag/N-TiO_2 nanojunction film for enhanced photogenerated charges utilization, Chem. Commun. 47 (2011) 8641–8643.
[4] M. Shang, W.Z. Wang, J. Ren, S.M. Sun, L. Zhang, Nanoscale Kirkendall effect for the synthesis of Bi_2MoO_6 boxes via a facile solution-phase method, Nanoscale 3 (2011) 1474–1476.
[5] G.H. Tian, Y.J. Chen, W. Zhou, K. Pan, Y.Z. Dong, C.G. Tian, H.G. Fu, Facile solvothermal synthesis of hierarchical flower-like Bi_2MoO_6 hollow spheres as high performance visible-light driven photocatalysts, J. Mater. Chem. 21 (2011) 887–892.
[6] W.Z. Yin, W.Z. Wang, S.M. Sun, Photocatalytic degradation of phenol over cage-like Bi_2MoO_6 hollow spheres under visible-light irradiation, Catal. Commun. 11 (2010) 647–650.
[7] T. Zhou, J. Hu, J. Li, Er^{3+} doped bismuth molybdate nanosheets with exposed {0 1 0} facets, enhanced photocatalytic performance, Appl. Catal. B: Environ. 110 (2011) 221–230.
[8] X. Zhao, H. Liu, Y. Shen, J. Qu, Photocatalytic reduction of bromate at C_{60} modified Bi_2MoO_6 under visible light irradiation, Appl. Catal. B: Environ. 106 (2011) 63–68.
[9] N. Li, L. Zhu, W.D. Zhang, Y.X. Yu, W.H. Zhang, M.F. Hou, Modification of TiO_2 nanorods by Bi_2MoO_6 nanoparticles for high performance visible-light photocatalysis, J. Alloys Compd. 47 (2011) 9770–9775.
[10] Z. Zhang, C. Shao, X. Li, L. Zhang, H. Xue, C. Wang, Y. Liu, Protein folding as flow across a network of folding-unfolding pathways. 1. The mid-transition case, J. Phys. Chem. C 114 (2010) 7920–7929.
[11] C. Wang, C. Shao, X. Zhang, Y. Liu, SnO_2 nanostructures-TiO_2 nanofibers heterostructures: controlled fabrication and high photocatalytic properties, Inorg. Chem. 48 (2009) 7261–7268.
[12] T. Cao, Y. Li, C. Wang, Z. Zhang, M. Zhang, C. Shao, Y. Liu, Bi_4Ti3O_{12} nanosheets/TiO_2 submicron fibers heterostructures: in situ fabrication and high visible light photocatalytic activity, J. Mater. Chem. 21 (2011) 6922–6927.
[13] U. Sulaeman, S. Yin, T. Sato, Solvothermal synthesis of designed nonstoichiometric strontium titanate for efficient visible-light photocatalysis, Appl. Phys. Lett. 97 (2010) 103102.
[14] P. Zhang, C. Shao, Z. Zhang, M. Zhang, J. Mu, Z. Guo, Y. Liu, TiO_2@carbon core/shell nanofibers: controllable preparation and enhanced visible photocatalytic properties, Nanoscale 3 (2011) 2943–2949.
[15] P. Zhang, C. Shao, Z. Zhang, M. Zhang, J. Mu, Z. Guo, Y. Liu, Core/shell nanofibers of TiO_2@carbon embedded by Ag nanoparticle with enhanced visible photocatalytic activity, J. Mater. Chem. 21 (2011) 17746–17753.
[16] D. Chen, H. Zhang, X. Li, J.H. Li, Biofunctional titania nanotubes for visible-light-activated photoelectrochemical biosensing, Anal. Chem. 82 (2010) 2253–2261.
[17] Y. Xu, C.H. Langford, UV-or visible-light-induced degradation of X3B on TiO_2 nanoparticles: the influence of adsorption, Langmuir 17 (2001) 897–902.

[18] X. Li, K. Lv, K. Deng, J. Tang, R. Su, J. Sun, L. Chen, Synthesis and characterization of ZnO and TiO_2 hollow spheres with enhanced photoreactivity, Mater. Sci. Eng. B 158 (2009) 40–47.
[19] A.H. Nethercot, Prediction of fermi energies and photoelectric thresholds based on electronegativity concepts, Phys. Rev. Lett. 33 (1974) 1088–1091.
[20] H. Zhang, X. Lv, Y. Li, D. Chen, L. Li, J.H. Li, P25-graphene composite as a high performance photocatalyst, ACS Nano 4 (2010) 380–386.
[21] M.C. Long, W.M. Cai, H. Kisch, Photoelectrochemical properties of nanocrystalline Aurivillius phase Bi_2MoO_6 film under visible light irradiation, Chem. Phys. Lett. 461 (2008) 102–105.
[22] H.X. Li, Z.F. Bian, J. Zhu, D.Q. Zhang, G.S. Li, Y.N. Huo, H. Li, Y.F. Lu, Mesoporous titania spheres with tunable chamber structure and enhanced photocatalytic activity, J. Am. Chem. Soc. 129 (2007) 8406–8407.
[23] G. Li, J. Liu, G. Jiang, Facile synthesis of spiny mesoporous titania tubes with enhanced photocatalytic activity, Chem. Commun. 47 (2011) 7443–7445.